

Topological design of electromechanical actuators with robustness toward over- and under-etching

Xiaoping Qian

Ole Sigmund

Department of Mechanical, Materials
and Aerospace Engineering
Illinois Institute of Technology
Chicago, IL 60062, USA
Email: qian@iit.edu

Department of Mechanical Engineering
Technical University of Denmark
DK-2800 Kgs. Lyngby, Denmark
Email: sigmund@mek.dtu.dk

In this paper, we combine the recent findings in robust topology optimization formulations and partial differential equation based density filtering to improve the topological design of electromechanical actuators. For the electromechanical analysis, we adopt a monolithic formulation to model the coupled electrostatic and mechanical equations. For filtering, we extend the Helmholtz-based projection filter with Dirichlet boundary conditions to ensure appropriate design boundary conditions. For the optimization, we use the Method of Moving Asymptotes, where the sensitivity is obtained from the adjoint approach.

Our study shows that the robust filter approach produces topology optimized actuators with minimal length control and crisp structural boundaries. In particular, the minimal length control of both structural features and gap widths avoids common modeling artifacts in topology optimization, i.e. one-element wide structural parts or gaps. It thus leads to physically realizable designs that are robust against manufacturing imprecision such as over- and under-etching.

Keywords Topology optimization, electromechanical actuator

1 Introduction

Design of multiphysics systems has become increasingly important for a variety of engineering applications. It is challenging to design such systems through engineer's intuition due to complex interactions between physics. Since its early inception [1, 2], topology optimization has been applied to a variety of multi-physics systems, particularly MEMS applications [3, 4, 5, 6, 7, 8, 9, 10]. This paper presents a robust formulation for topology optimization of nonlinear, coupled electromechanical systems actuated by Coulomb's (electrostatic) forces and is an extension and improvement of the work presented in [10]. The added robust formulation leads to optimized structures with clear black/white (almost no gray) boundaries and with minimal length scale control for both solid and void features. The minimal length scale control improves both mechanical and electrical analysis for topology optimization so that one-node hinges in electrodes or one-element gaps between electrodes that otherwise commonly exist in optimized designs are avoided.

Electrostatics is a simple case of electromagnetism where an electric field is considered as quasistatic due to stationary electric charges [11]. Most of the widely used MEMS devices use the

electrostatic phenomenon for actuation, such as comb-drive actuators and sensors consisting of integrated capacitors [12, 13]. In a quasistatic electric field, a structure will be subjected to electrostatic force due to induced charges on structural surfaces. This electrostatic force in turn leads to structural deformation. Because the deformation of the structure influences the electric field and the resulting electrostatic force, the coupling between the electric field and the structural displacement must be considered simultaneously [6, 8]. In this paper, our analysis is based on a monolithic formulation of the coupled electromechanical analysis [10], rather than typical staggered analyses for coupled problems. The minimal length of both solids and gaps in optimized designs is obtained by solving three sets of such coupled electric and elastic equations with the material density filtered by the Helmholtz partial differential equation based filter. Our study finds that such obtained minimal lengths in optimized designs agree remarkably well with minimal length predicted through the numerical approach [14] or an analytical formula (derived in the Appendix).

The remainder of this paper is organized as follows. Section 2 reviews the monolithic formulation of electromechanical analysis. Section 3 describes the robust formulation of topology optimization under coupled electromechanical governing partial differential equations (PDEs). Section 4 presents how Helmholtz PDE filter under Dirichlet boundary conditions can be implemented. Section 4 details the numerical results on the optimization of an electrostatic displacement inverter and a gripper. The paper is concluded in Section 5.

2 Monolithic formulation of electro-mechanical equations in the undeformed domain

This paper adopts a monolithic approach for coupled electromechanical analysis first suggested in Ref. [10]. For the sake of self-containedness, we briefly outline this approach in the following. For details, see [10]. This approach is amenable to topology optimization by avoiding many obstacles in the usual staggering analysis approach to coupled problems. More specifically,

- It allows unified equations for modeling both semi-conductors (e.g. silicon) and insulators (e.g. air), thus avoiding alternating physics as in the staggering analysis approach. It uses SIMP material interpolation functions for three material properties in the unified domain: Young's modulus C in the linear elasticity equation, generalized permittivity $\tilde{\epsilon}$ in the electric Poisson equation, and the permittivity ϵ for the electrostatic force calculations.
- The electrostatic forces are calculated by volume integration instead of usual surface integration of Maxwell's stress tensor due to the absence of explicit representation of structural boundary in topology optimization.
- Governing equations are transformed from the deformed domain to the undeformed domain using the deformation tensor so that no re-meshing or mesh morphing is required in the optimization process.

Using the generalized permittivity $\tilde{\epsilon}(\mathbf{x})$, we can set up the electric equation as,

$$\nabla_{\mathbf{x}} \cdot (\tilde{\epsilon}(\mathbf{x}) \nabla_{\mathbf{x}} p) = 0 \quad \text{in } {}^t\Omega(\mathbf{u}) \quad (1)$$

where ${}^t\Omega(\mathbf{u})$ represents the deformed domain and p is the electric potential. The generalized permittivity is so chosen that it can model both semi-conductor and insulator simultaneously (c.f.

[10]). For semi-conductors, a constant potential exists on all surfaces. The particular form of the permittivity interpolation shall be discussed later.

The linear elasticity equation including prestress from the Maxwell's stress tensor is

$$\begin{cases} \nabla_{\mathbf{x}} \cdot \mathbf{T} + \nabla_{\mathbf{x}} \cdot \mathbf{T}_E = 0 & \text{in } {}^t\Omega(\mathbf{u}) \\ \mathbf{T} = \mathbf{C}\mathbf{S} \\ \mathbf{S} = \frac{1}{2}(\nabla_{\mathbf{x}}^T \mathbf{u} + \nabla_{\mathbf{x}} \mathbf{u}) \end{cases} \quad (2)$$

where \mathbf{T}_E is the Maxwell's stress tensor, \mathbf{T} is the stress, \mathbf{S} is the strain, \mathbf{u} is displacement, and the deformation-independent constitutive matrix is denoted as \mathbf{C} . Note that for the stress, we assume geometrically linear analysis, i.e. we neglect changes of surface areas, volumes and mass densities between deformed and undeformed structural domains [15]. Hence, we have

$$\nabla_{\mathbf{x}} \cdot \mathbf{T} = \nabla_{\mathbf{X}} \cdot \mathbf{T}. \quad (3)$$

where \mathbf{x} and \mathbf{X} represent space coordinates after and before the deformation, respectively. The Maxwell's stress tensor is calculated as follows

$$\mathbf{T}_E = \varepsilon(\mathbf{x}) \left(\mathbf{E}\mathbf{E} - \frac{\mathbf{E} \cdot \mathbf{E}}{2} \mathbf{I} \right) \quad (4)$$

with the electric field $\mathbf{E} = -\nabla_{\mathbf{x}} p$.

Combining (1) and (2), we obtain the following weak form of the electric and elastic equations in the deformed domain: find p and \mathbf{u} such that

$$\int_{{}^t\Omega} (\nabla_{\mathbf{x}} \delta p)^T \cdot (\tilde{\varepsilon}(\mathbf{x}) \nabla_{\mathbf{x}} p) \, d\Omega = 0, \quad (5)$$

$$\int_{0\Omega} \delta \mathbf{S}^T \cdot \mathbf{T} \, d\Omega = - \int_{{}^t\Omega} \delta \mathbf{S}(\mathbf{u}, \delta \mathbf{u})^T \cdot \mathbf{T}_E \, d\Omega, \quad (6)$$

where δp is the test function for the electric potential p , $\delta \mathbf{S}$ is the test function (virtual strain) for strain \mathbf{S} with $\delta \mathbf{S}(\mathbf{u}) = \frac{1}{2}(\nabla_{\mathbf{X}} \delta \mathbf{u}^T + \nabla_{\mathbf{X}} \delta \mathbf{u})$ and $\delta \mathbf{S}(\mathbf{u}, \delta \mathbf{u}) = \frac{1}{2}(\nabla_{\mathbf{x}} \delta \mathbf{u}^T + \nabla_{\mathbf{x}} \delta \mathbf{u})$. Note that the linear structural potential energy is represented directly in the undeformed domain, as assumed earlier. We can transform the other integral forms from the deformed domain into the undeformed domain via the deformation tensor $\mathbf{F} = \frac{\partial \mathbf{x}}{\partial \mathbf{X}}$. Using $\nabla_{\mathbf{x}} \mathbf{u} = \mathbf{F}^{-T} \nabla_{\mathbf{X}} \mathbf{u}$, $\nabla_{\mathbf{x}} p = \mathbf{F}^{-T} \nabla_{\mathbf{X}} p$, $\int_{{}^t\Omega} (\cdot) \, d\Omega = \int_{0\Omega} (\cdot) \|\mathbf{F}\| \, d\Omega$ and $\delta \mathbf{S}(\mathbf{u}, \delta \mathbf{u}) = \frac{1}{2}((\mathbf{F}^{-T} \nabla_{\mathbf{X}} \delta \mathbf{u})^T + \mathbf{F}^{-T} \nabla_{\mathbf{X}} \delta \mathbf{u})$, we thus have the weak form in the undeformed domain, find $p \in P$ and $\mathbf{u} \in U$ such that

$$\int_{0\Omega} (\nabla_{\mathbf{X}} \tilde{p})^T (\mathbf{F}^{-1} \tilde{\varepsilon}(\mathbf{X}) \mathbf{F}^{-T}) \nabla_{\mathbf{X}} p \|\mathbf{F}\| \, d\Omega = 0, \quad \forall \tilde{p} \in P_0 \quad (7)$$

$$\int_{0\Omega} \tilde{\mathbf{S}}^T \cdot \mathbf{T} \, d\Omega + \int_{0\Omega} \tilde{\mathbf{S}}(\mathbf{u}, \tilde{\mathbf{u}})^T \cdot \mathbf{T}_E \|\mathbf{F}\| \, d\Omega = 0, \quad \forall \tilde{\mathbf{u}} \in U_0. \quad (8)$$

where

$$P = \{p | p \in H^1(\Omega), p = \bar{p} \text{ on } \Gamma_p\}$$

$$\begin{aligned}
P_0 &= \{\tilde{p} | \tilde{p} \in H^1(\Omega), \tilde{p} = 0 \text{ on } \Gamma_p\} \\
U &= \{\mathbf{u} | \mathbf{u} \in H^1(\Omega), \mathbf{u} = \bar{\mathbf{u}} \text{ on } \Gamma_u\} \\
U_0 &= \{\tilde{\mathbf{u}} | \tilde{\mathbf{u}} \in H^1(\Omega), \tilde{\mathbf{u}} = 0 \text{ on } \Gamma_u\}
\end{aligned}$$

The above weak form is solved by the finite element method in this paper. Upon discretization, it leads to residual equations $\mathbf{R}(\mathbf{u}) = 0$ corresponding to the non-linear finite element implementation of eqs (7) and (8).

3 Robust topology optimization

In the original work on the monolithic topology optimization formulation for electrostatic mechanism design [10], it was quite a challenge to enforce strict length-scales in gap regions. Obviously, one element wide gap regions with significant jumps in electric potential do not represent physical reality well. In order to partially alleviate this problem, ref. [10] suggested to use the modified Heaviside projection scheme [16], a scheme that for simple compliance problems works very well and ensures minimum length scale control for void regions. For the electromechanical actuator design problem this scheme did ensure finite gap regions to a certain extent, however, problems with enforcing strictly solid-void designs resulted in somewhat unsatisfactory modeling of the electric field in gap regions. Also, the modified Heaviside filtering only controls void length scales, hence it was not able to prevent thin and non-physical hinge regions.

Lately, so-called robust filtering approaches have shown great promise [17, 14] in preventing small details and ensuring finite length scales for minimum compliance and compliant mechanism design problems. Apart from ensuring strict control of both solid and void length scales, numerical experiments indicate that the robust filtering concept, that entails optimization of three different design realizations (the blue-print design as well as the under- and over-etched realizations), yields an intrinsic penalization of grey regions.

Based on above observations, we find it worthwhile to revisit the challenging problem of electrostatic compliance mechanism design and to combine it with the newest findings in robust topology optimization approaches to result in a design methodology that ensures physically meaningful simulations and results.

3.1 Robust formulation of topology optimization

The specifications of topological design of the electromechanical actuator are shown in Fig 1. That is,

$$\left\{ \begin{array}{l} \min_{\rho} \quad J = -k_s u_2^A \\ \text{s.t.} \quad \frac{V}{V_0} - \beta \leq 0 \\ \mathbf{R}(\mathbf{u}(\rho), \rho) = 0 \\ 0 \leq \rho \leq 1 \end{array} \right. \quad (9)$$

where u_2^A is the vertical displacement of point A and $\mathbf{R}(\mathbf{u}(\rho), \rho) = 0$ is the residual equation representing the coupled electromechanical system with material density parameterized by ρ . The design objective is to maximize the force applied to the output spring subject to a volume constraint.

To control the output force and displacement behavior, a small spring stiffness k_s is added to point A along the vertical direction.

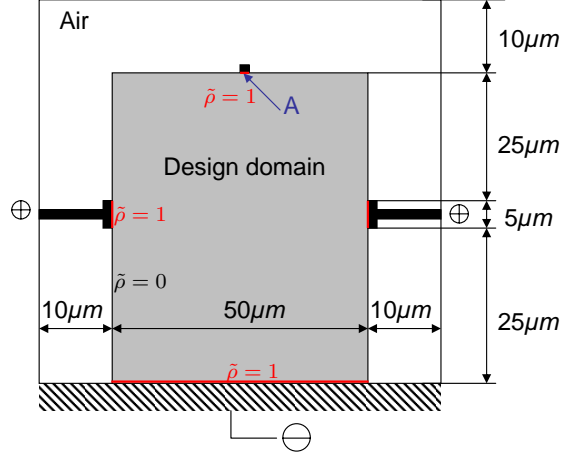


Figure 1: Design specifications for topology optimization of an electromechanical inverter. The shaded area is the design domain. The red bold lines mark the fixed design variables $\rho = 1$, which are used to indicate the input voltage port and the output port.

The basic idea of the robust filter for topology optimization [14] is to minimize the maximum of the cost functions of three design realizations, corresponding to the eroded, the intermediate (blue-print) and the dilated structures. These three structures are represented by one set of design variables ρ but with three different thresholds, $1 - \eta$, 0.5 , η , in the Heaviside projection filter [18, 16, 19]. This robust filter can be considered as a worst-case robust filter. The specific formulation of the robust filter is as follows.

$$\begin{aligned}
& \min_{\rho} \max(J(\bar{\rho}^e(\rho)), J(\bar{\rho}^i(\rho)), J(\bar{\rho}^d(\rho))) \\
& \text{s.t. } \mathbf{R}(\mathbf{u}^e(\bar{\rho}^e(\rho)), \bar{\rho}^e(\rho)) = 0 \\
& \quad \mathbf{R}(\mathbf{u}^i(\bar{\rho}^i(\rho)), \bar{\rho}^i(\rho)) = 0 \\
& \quad \mathbf{R}(\mathbf{u}^d(\bar{\rho}^d(\rho)), \bar{\rho}^d(\rho)) = 0 \\
& \quad V(\bar{\rho}^d(\rho)) \leq V^* \\
& \quad 0 \leq \rho \leq 1
\end{aligned} \tag{10}$$

where $J = -k_s u_2^A$ is implicitly defined as functions of design variables ρ by solving the state residual equations $\mathbf{R}(\mathbf{u}(\rho), \rho) = 0$. The physical material densities $\bar{\rho}$ are found from a Heaviside projection of the filtered variable field $\tilde{\rho}$ with the different threshold values corresponding to the three different design realizations. The optimization formulation in (10) is solved with a bound formulation [20] via the method of moving asymptotes (MMA) [21]. The sensitivity is obtained through the adjoint method in COMSOL [10, 22]. More details on the filtering technique are given in Section 4.

3.2 Material interpolation functions

The interpolation between material properties of air and solid regions are given by the standard SIMP (Simplified Isotropic Material with Penalization) scheme

$$\begin{aligned}\varepsilon(\rho) &= (\varepsilon_s - \varepsilon_a)\bar{\rho}^n + \varepsilon_a \\ \tilde{\varepsilon}(\rho) &= (\tilde{\varepsilon}_s - \tilde{\varepsilon}_a)\bar{\rho}^n + \tilde{\varepsilon}_a \\ C(\rho) &= (C_s - C_a)\bar{\rho}^n + C_a,\end{aligned}\tag{11}$$

where subscript s and a on material properties refer to solid and air regions, respectively. The penalty parameter n is chosen as 3 in this paper.

3.3 Volume constraint

Note here that the volume constraint in (10) is imposed on the dilated design $\bar{\rho}^d(\rho)$. The volume constraint's sensitivity can be obtained via the integral of each node's shape function [22]. More specifically, from the volume constraint in (9), we have

$$g = \frac{\int_{\Omega} \bar{\rho} \, d\Omega}{V_0} - \gamma \leq 0\tag{12}$$

where $V_0 = \int_{\Omega} d\Omega$ is the volume of the design domain and γ is the allowed volume fraction of the material. Then the discretized sensitivity of the volume constraint becomes

$$\frac{\partial g}{\partial \bar{\rho}_i} = \frac{\int_{\Omega} N_i \, d\Omega}{V_0}\tag{13}$$

where N_i is the shape function for each density node i . Note that, in our implementation, the material density field is represented via linear quadrilateral elements with each node corresponding to one density variable and the element interior interpolated through the nodal shape functions. Similar usage of approximation of material distribution has been reported in [23, 24]. However, a model with piece-wise constant element densities would have shown similar results.

4 Helmholtz PDE based density filter with Dirichlet boundary conditions

The Helmholtz filtering approach [25, 26] is a PDE-based realization of the popular sensitivity and density filtering approaches for ensuring length-scale control in topology optimization. The filter is volume preserving and, compared to the image-processing inspired filtering approaches, it avoids explicit storing of neighboring information of the mesh. Further, the filtering is amenable to parallel computing, c.f. [26].

Isotropic Helmholtz PDE filtering can be described as

$$-r^2 \nabla^2 \tilde{\rho} + \tilde{\rho} = \rho\tag{14}$$

where r controls the size of the integral kernel, ρ is the input design variable field and $\tilde{\rho}$ is the filtered field. By comparing the second moment of the Green's functions of the Helmholtz PDE with that

of the normalized hat weighting functions used in standard filtering techniques, the relationship between the length scales is [26]

$$R = 2\sqrt{3} r$$

where R corresponds to the effective filter radius in standard filtering techniques.

The weak form of (14) is

$$\int_{\Omega} r^2 \nabla v \nabla \tilde{\rho} + v(\tilde{\rho} - \rho) \, d\Omega = 0, \quad (15)$$

where v is the test function for $\tilde{\rho}$. In discrete FEM terms, this can be written as

$$\mathbf{K}\tilde{\boldsymbol{\rho}} = \mathbf{T}\boldsymbol{\rho} \quad (16)$$

$$\mathbf{K} = \sum_e \int_{\Omega_e} \nabla \mathbf{N}^T r^2 \nabla \mathbf{N} + \mathbf{N}^T \mathbf{N} \, d\Omega \quad (17)$$

$$\mathbf{T} = \sum_e \int_{\Omega_e} \mathbf{N}^T \mathbf{N} \, d\Omega \quad (18)$$

where \mathbf{N} is the element shape functions, $\boldsymbol{\rho}$ is the nodal density before the filtering, $\tilde{\boldsymbol{\rho}}$ is the nodal density after the filtering and \sum is the standard FE assembly operation. If we define the stiffness matrix \mathbf{K} as a function of the length scale r , we then have the following relationship between the stiffness matrix \mathbf{K} and mass-like matrix \mathbf{T} :

$$\mathbf{T} = \mathbf{K}(0). \quad (19)$$

Since the matrices \mathbf{K} and \mathbf{T} do not change during design iteration, they can be pre-computed and pre-factorized before the optimization iterations.

In its standard setting, the Helmholtz filtering approach uses Neuman boundary conditions for the filtered variables $\tilde{\rho}$ [27]. However, for problems with prescribed regions of solid and void material, one must add Dirichlet conditions to ensure appropriate fulfillment of length-scale constraints at these boundaries. Hence, as shown in Fig. 1 we specify material as solid at the input and output ports (i.e. $\tilde{\rho} = 1$), void at exterior boundaries (i.e. $\tilde{\rho} = 0$) and we only impose Neuman (free) boundary conditions at symmetric boundaries.

With the Dirichlet boundary conditions, the discrete FE equations become

$$\begin{bmatrix} \mathbf{K}_E & \mathbf{K}_{EF} \\ \mathbf{K}_{EF}^T & \mathbf{K}_F \end{bmatrix} \begin{bmatrix} \tilde{\boldsymbol{\rho}}_E \\ \tilde{\boldsymbol{\rho}}_F \end{bmatrix} = \begin{bmatrix} \mathbf{f}_E + \mathbf{r}_E \\ \mathbf{f}_F \end{bmatrix} \quad (20)$$

where $\mathbf{f}_F = \mathbf{T}_F \boldsymbol{\rho}_F + \mathbf{T}_{EF}^T \boldsymbol{\rho}_E$, and f_E and r_E are prescribed and reaction forces at the essential DOFs [28]. Note that we have separated DOFs $\tilde{\boldsymbol{\rho}}$ into $\tilde{\boldsymbol{\rho}}_E$ (essential, prescribed values) and $\tilde{\boldsymbol{\rho}}_F$ (free, unknown values), and likewise for $\boldsymbol{\rho}$. We can thus obtain the solution to the unknowns $\tilde{\boldsymbol{\rho}}_F$ via the elimination method as

$$\begin{aligned} \mathbf{K}_F \tilde{\boldsymbol{\rho}}_F &= \mathbf{T}_F \boldsymbol{\rho}_F + \mathbf{T}_{EF}^T \boldsymbol{\rho}_E - \mathbf{K}_{EF}^T \tilde{\boldsymbol{\rho}}_E, \\ \tilde{\boldsymbol{\rho}}_F &= \mathbf{K}_F^{-1} \mathbf{T}_F \boldsymbol{\rho}_F + \underbrace{\mathbf{K}_F^{-1} (\mathbf{T}_{EF}^T \boldsymbol{\rho}_E - \mathbf{K}_{EF}^T \tilde{\boldsymbol{\rho}}_E)}_{\tilde{\boldsymbol{\rho}}_0}, \end{aligned} \quad (21)$$

where $\tilde{\boldsymbol{\rho}}_0$ can be obtained from the PDE solver for solving $\tilde{\boldsymbol{\rho}}_F$ by setting $\boldsymbol{\rho}_F = 0$.

From (21), we thus have

$$\tilde{\boldsymbol{\rho}}_F = \mathbf{K}_F^{-1} \mathbf{T}_F \boldsymbol{\rho}_F + \tilde{\boldsymbol{\rho}}_0 \quad (22)$$

where $\tilde{\boldsymbol{\rho}}_0$ is independent from $\boldsymbol{\rho}_F$. The sensitivity of the Helmholtz filter is

$$\frac{\partial \tilde{\boldsymbol{\rho}}_F}{\partial \boldsymbol{\rho}_F} = \mathbf{T}_F^T \mathbf{K}_F^{-1}, \quad (23)$$

where we have utilized the symmetry of \mathbf{K}_F . The sensitivities of any function $f(\tilde{\boldsymbol{\rho}}_F)$ as in (10) over the design variables $\boldsymbol{\rho}_F$ can then be obtained as follows

$$\frac{\partial f}{\partial \boldsymbol{\rho}_F} = \frac{\partial f}{\partial \tilde{\boldsymbol{\rho}}_F} \frac{\partial \tilde{\boldsymbol{\rho}}_F}{\partial \boldsymbol{\rho}_F} \quad (24)$$

where $\tilde{\rho}$ is the Heaviside filtered density found as

$$\tilde{\rho}_i = \frac{\tanh(\beta\eta) + \tanh(\beta(\tilde{\rho}_i - \eta))}{\tanh(\beta\eta) + \tanh(\beta(1 - \eta))} \quad (25)$$

The coefficient η determines the threshold level. For $\eta = 0$, the projection corresponds to the original Heaviside projection concept [18], for $\eta = 1$ we have the modified Heaviside projection concept [16] and for $\eta = 1/2$ we have the volume preserving projection concept [19]. The robust formulation makes use of three separate projections in each design step, hence η is substituted with the three values $1 - \eta$, 0.5 , η with $\eta \in [0, 0.5]$, denoting the eroded, the blue-print and the dilated realization, respectively. The coefficient β determines the degree of discreteness of the smoothed Heaviside function. In numerical experiments, the value of β is initialized to 1 and then doubled every 50th iteration until it reaches 128, whereafter the coefficient is held constant until final convergence.

Finally, inserting (23) in (24), we get the sensitivity of any function $f(\tilde{\boldsymbol{\rho}})$ over design variable $\boldsymbol{\rho}$ as

$$\frac{\partial f}{\partial \boldsymbol{\rho}_F} = \mathbf{T}_F^T \mathbf{K}_F^{-1} \frac{\partial f}{\partial \tilde{\boldsymbol{\rho}}_F} \frac{\partial \tilde{\boldsymbol{\rho}}_F}{\partial \boldsymbol{\rho}_F}. \quad (26)$$

5 Numerical results

In this section, we present the robust topological optimization of two kinds of electromechanical actuators: a displacement inverter and a gripper. Our implementation is based on Matlab scripts with analysis done in COMSOL 4.2 and optimization via MMA [21].

In this paper, Young's modulus for the solid (Silicon) is $C_s = 153\text{GPa}$ and for the void is $C_a = C_s/10^4$ where the stiffness contrast between the two materials is 10^4 . The Poisson ratio is 0.17 and the spring stiffness in both examples are chosen to be $k_s = 40\mu\text{N}/\mu\text{m}$. The relative permittivity of solid is $\varepsilon_s = 10\varepsilon_0$ and of air is $\varepsilon_a = \varepsilon_0$. The generalized permittivity for solid is $\tilde{\varepsilon}_s = 10^5\varepsilon_0$ and for air it is $\tilde{\varepsilon}_a = \varepsilon_0$. Except for the minimum stiffness value all the parameters used in the examples are physically realistic. The choice of the minimum stiffness value, however, is rather critical. A too large value yields artificial stiffness in void regions and a too small value sometimes causes instability problems. We believe that the latter problem can be alleviated by introducing snap-through constraints as used in refs [5, 6]. However, since the emphasis is on geometry control rather than on exact physical modeling we have not included this option in the

present study The penalty factors for all material interpolations (11) are $n = 3$. The volume fraction $\gamma = 0.3$. The convergence criteria is that the maximum change of each design variable between two consecutive iterations should be smaller than 0.01. In all cases reported in this paper, the optimization converges in 400 \sim 700 iterations.

5.1 Robust inverter design

In the following, we present the numerical result for the inverter problem specified in Fig. 1. Note that during the modeling, symmetry is used to reduce analysis time. A total of 20,475 bilinear quadrilateral elements are used in the analysis of half the design domain with each element of size $0.3333\mu\text{m} \times 0.3333\mu\text{m}$.

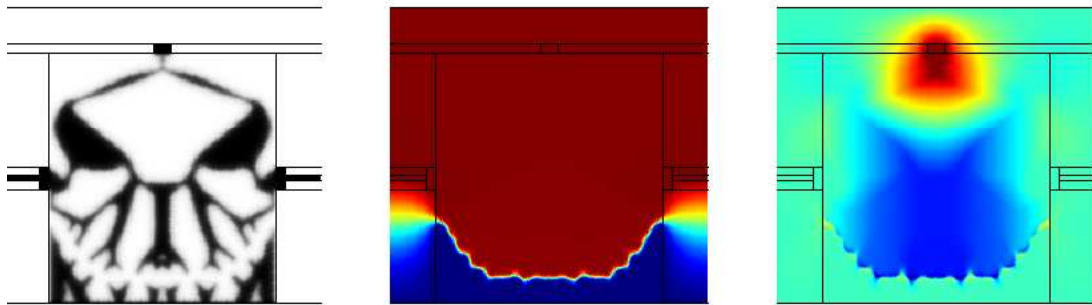
5.1.1 Optimization without the robust filter

We first present the optimized design without the robust filter, i.e. under the Helmholtz PDE filter and the simple projection filtering with $\eta = 0.5$ corresponding to the volume preserving Heaviside projection proposed in Ref. [19]. Figure 2a shows the optimized design with the Helmholtz PDE filter as the density filter and the corresponding electric potential and vertical displacement for the design are shown in Figure 2b and Figure 2c. The resulting objective function is $J = -0.0143\mu\text{N}$. Figure 2d and Figure 2g show two optimized designs and their electric potential and vertical displacement under the simple Heaviside filter with filter sizes $R = 6.3h$ and $R = 8.4h$ with h being the element length. From the optimized actuators, we can see that, although the resulting objective functions are $-0.1938\mu\text{N}$ and $-0.1944\mu\text{N}$, the optimized designs possess single-node-connected hinges as well as one-element wide narrow gaps that may not be physically realizable. This confirms that the volume preserving Heaviside filter strategy does not provide any length-scale control, neither for solid regions, nor for voids. This corresponds to the conclusions from Ref. [14]. From the potential distribution (Fig. 2e and Fig. 2h), it is clear that there is sharp transition between input voltage and ground voltage due to the tiny gap between the electrodes. By increasing the filter radius, these single-node hinges and single-element gaps between electrodes still exist.

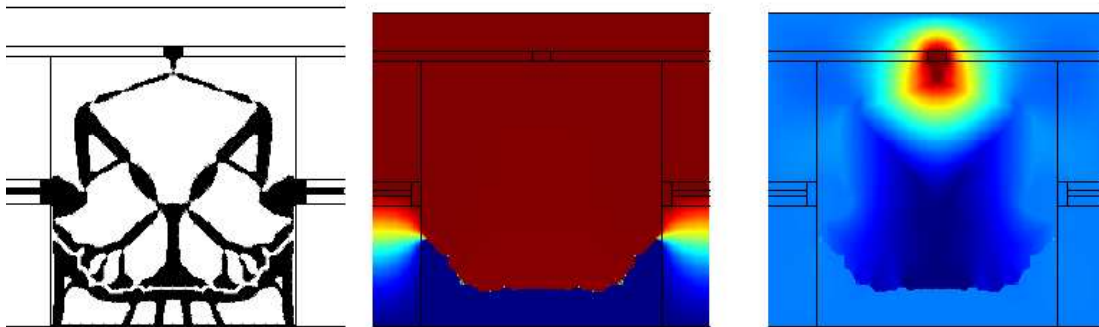
Figure 3 give a more detailed illustration of the single-node hinge and single-element gap issue for the actuator designs in Fig. 2. In subfigures 3b, 3c, 3e and 3f, each square represents one quadrilateral element. Note that the slanted lines split each element into two triangles for surface rendering. Figure 3b shows the single-node hinge corresponding to a dashed rectangle in Fig. 3a. Figure 3c shows the single-element electrode gap corresponding to a thin tube in Fig. 3a. In Fig. 3c, the color trend of the tube represents the potential distribution. From this subfigure, one can see that the voltage changes from 0V to 50v in $0.3333\mu\text{m}$, i.e. in one element. A similar graphical illustration for the actuator design in Fig. 2b is shown in the second row of Fig. 3. Again, the single-node hinge and single-element gap issues persist even though the filter radius has been increased from 6.3 elements to 8.4 elements wide. Such thin hinges and gaps thus lead to poor mechanical and electric modeling and do not represent the underlying physics well.

5.1.2 Optimization with the robust filter

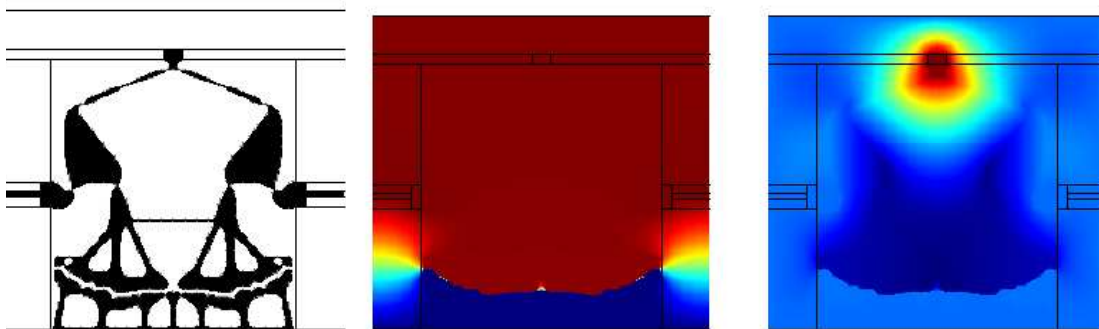
An optimized design obtained using the robust formulation is shown in Figure 4. Fig. 4a and Fig. 4b show the optimized design for $R = 8.4h, \eta = 0.25$, represented by the design variable field ρ



(a) Optimized inverter ($J = -0.0143\mu\text{N}$) with the Helmholtz PDE filter at $R = 6.3h$ (b) Electric potential for the design in Fig. 2a (c) Vertical displacement for the design in Fig. 2a



(d) Optimized inverter ($J = -0.1938\mu\text{N}$) with Heaviside filter in Fig. 2a at $R = 6.3h$ (e) Electric potential for the design in Fig. 2a (f) Vertical displacement for the design in Fig. 2a



(g) Optimized inverter ($J = -0.1944\mu\text{N}$) with Heaviside filter in Fig. 2b at $R = 8.4h$ (h) Electric potential for the design in Fig. 2b (i) Vertical displacement for the design in Fig. 2b

Figure 2: Optimized actuators and the corresponding potential and vertical displacement from the Helmholtz PDE filter and subsequent simple Heaviside filtering with $R = 6.3h$ and $R = 8.4h$.

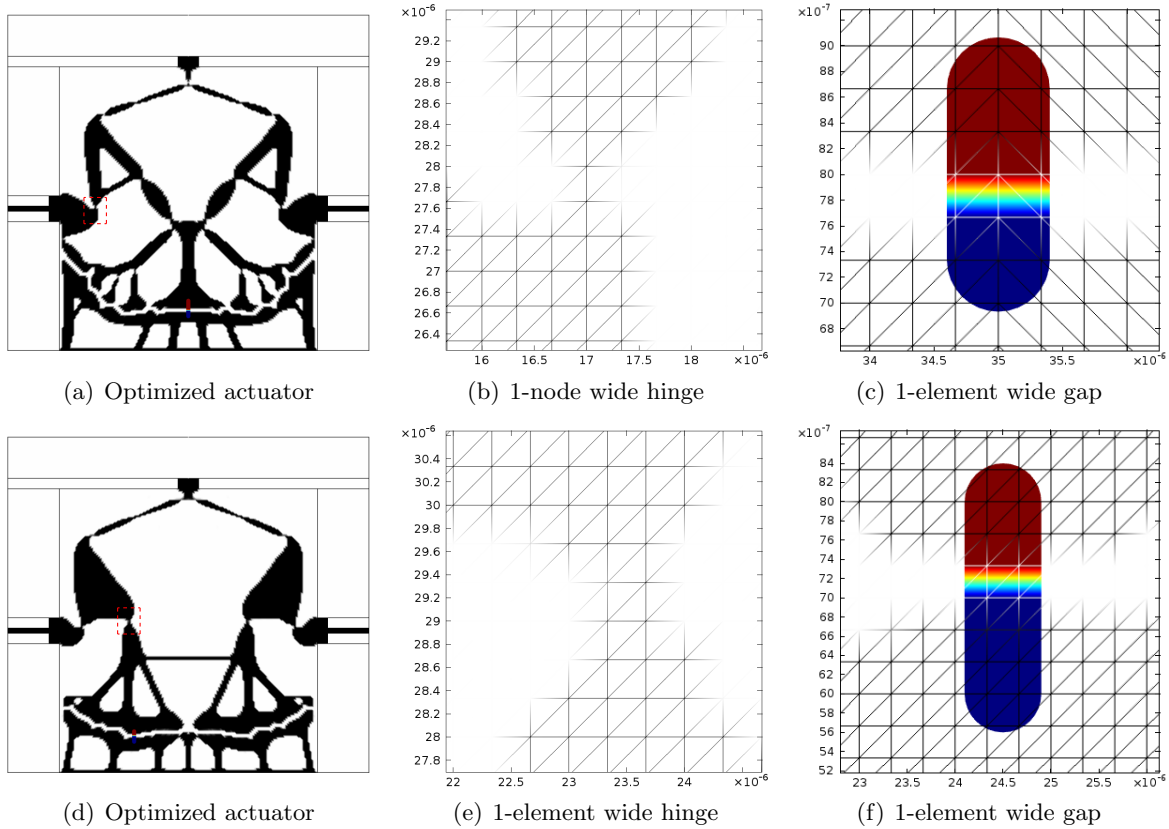


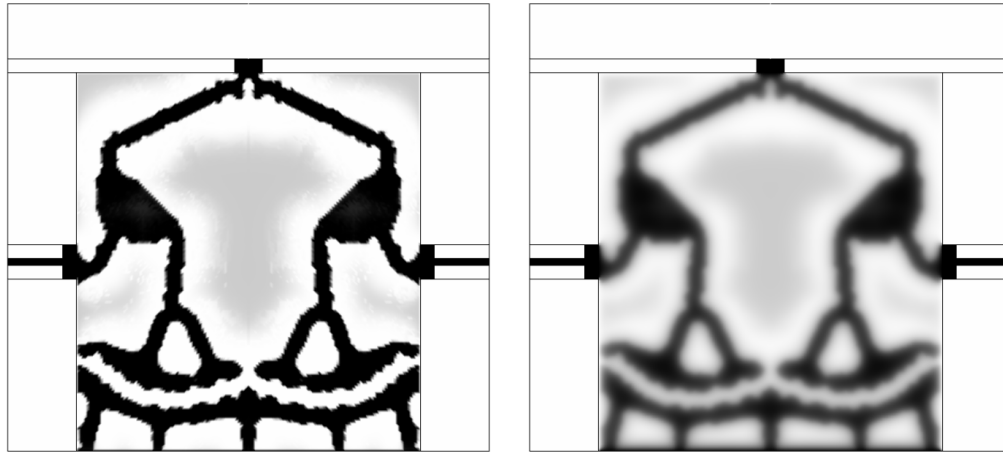
Figure 3: Magnified view of thin hinges and gaps in optimized designs in Fig. 2 that are obtained from simple Heaviside filter with filter radius $R = 6.3h$ (top row) and $R = 8.4h$ (second row). Fig. 3b and 3e are zoom-in of hinges (dotted rectangles) in 3a and 3d. Fig. 3c and 3f are zoom-in of gaps at small capsules in 3a and 3d. Fig. 3c and 3f also overlay the electric potential from Fig. 2e and 2h on top of the density profiles near the gap to show that the electric potential transitions in one element. Both designs exhibit thin hinges and gaps, resulting in poor mechanical and electric modeling.

and the Helmholtz filtered variable field $\tilde{\rho}$. From Fig. 4b, we can see that the Dirichlet boundary conditions for the PDE filters shown as red bold lines in Fig. 1 are satisfied. The left column of Fig. 4c shows the Heaviside filtered design $\tilde{\rho}$ under the thresholds $1 - \eta, 0.5, \eta$ and the middle column and the right column show the electrical potential and the vertical displacement of the domain. The caption above each subplot in Fig. 4c shows the number of iteration required for convergence (696 in this design) and the character (“i”, “e”, “d”) that follows refers to density, electric potential and vertical displacement for the eroded, intermediate and dilated structures, respectively. Among the three designs involved in the robust formulation, the intermediate one $\tilde{\rho}^i$ is used for the blue-print sent to fabrication. Even for rather large fabrication errors in the form of under- or over-etching the realized device should maintain good functionality. In the remainder of this paper, we display only the results for the intermediate (blue-print) design. Figure 5 shows the optimized design with filter size $R = 6.3h$ and $\eta = 0.25$.

The iteration history for the two designs are respectively shown in Fig. 6 and Fig. 7 where the history of objective functions (forces) and volume fractions for eroded, intermediate and dilated structures over the iterations are plotted. The forces and volume fractions for the intermediate structures are shown in bold lines, those of the eroded structures are shown in dashed lines and those of dilated structures are shown in thin lines. The convergence criteria is that the maximum change of density should be smaller than 0.01 in order to obtain a converged design and β should be no smaller than 128 to suppress the gray density in the optimized design. The design with $R = 8.4h$ converges in 696 iterations and the design with $R = 6.3h$ converges in 538 iterations. These two figures show that, in the early stage of optimization (within 150 iterations where $\beta < 8$), the forces for eroded, intermediate and dilated structures differ significantly and these differences can be seen visually from Fig. 6a and Fig. 7a. This is because at this stage all structures contain significant amount of gray densities (since $\beta < 8$) and thus leading to substantial differences in the forces. As the iteration progresses, the forces for the three structures become nearly identical since the maximum of the forces of the three structures is minimized. It should also be noted that, during the iteration, there are spikes at every 50-th iteration until 350 iterations. This is because β is doubled every 50 iterations until it reaches 128 which corresponds to the 350-th iteration. In contrast to previous work on robust compliant mechanism design [14] where only the eroded and the dilated structures were active in the optimization process we here have all three realizations active at the same time. This is attributed to the more complex physics involved in the electrostatic actuator case.

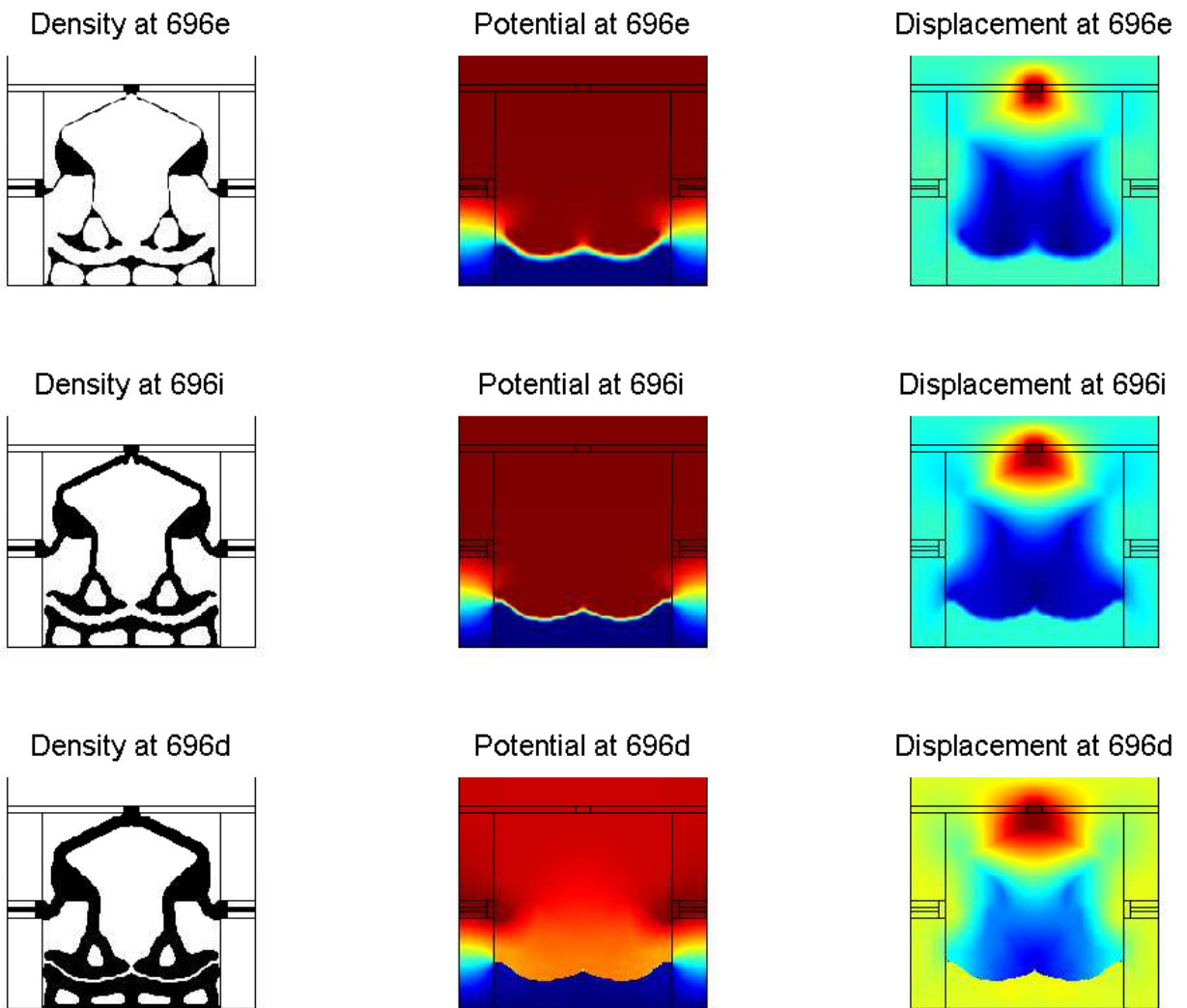
In order to better visualize the minimal length scale control of hinges and the electrode gap, Fig. 8 shows a magnified view of hinge and gap widths for the two designs in Figs. 4 and 5. It can be seen that both hinges and electrode gap span several elements.

In order to more quantitatively examine the length-scale control of minimal features from the filter size R and threshold η , we conducted a set of numerical experiments. Figure 9 shows six obtained design for length control with $R = 6.3h, 8.4h$ and $\eta = 0.2, 0.25, 0.35$. The dashed boxes indicate where the minimal hinges are measured and the colored thin tubes indicate where the gaps between electrodes are measured. This figure shows, as the threshold η decreases, the minimal hinge width and the gap increase and the cost function (inverting force) becomes smaller accordingly. Figure 10 plots the electric potential transitions between the electrode gaps in the six designs (in regions shown as thin tubes in Fig. 9). Each vertical grid line corresponds to an element separation of $0.33\mu m$. It is clear that, with the increase of filter radius R and the decrease of η , the electrode gaps become wider.



(a) Design variable field ρ

(b) PDE filtered field $\tilde{\rho}$



(c) Heaviside projected designs $\tilde{\rho}^e, \tilde{\rho}^i, \tilde{\rho}^d$, their electric potential and displacement

Figure 4: Optimized inverter with $R = 8.4h, \eta = 0.25$. a) design variable field ρ . b) PDE filtered variables $\tilde{\rho}$, c) three Heaviside filtered designs $\tilde{\rho}^e, \tilde{\rho}^i, \tilde{\rho}^d$.

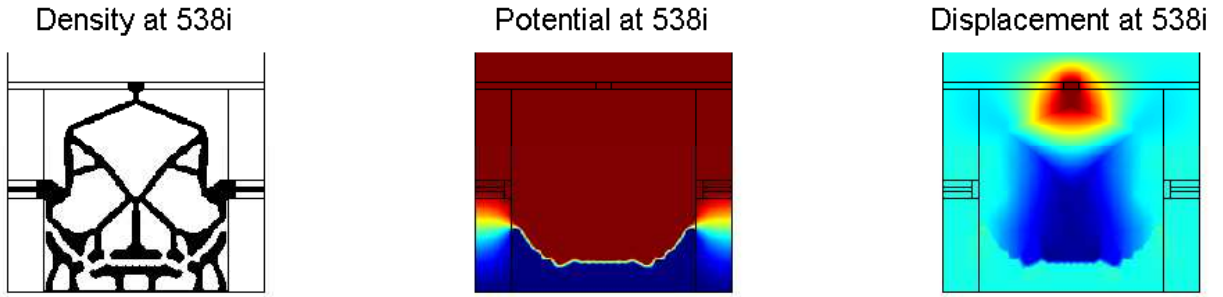


Figure 5: Optimized design with $R = 6.3h, \eta = 0.25$

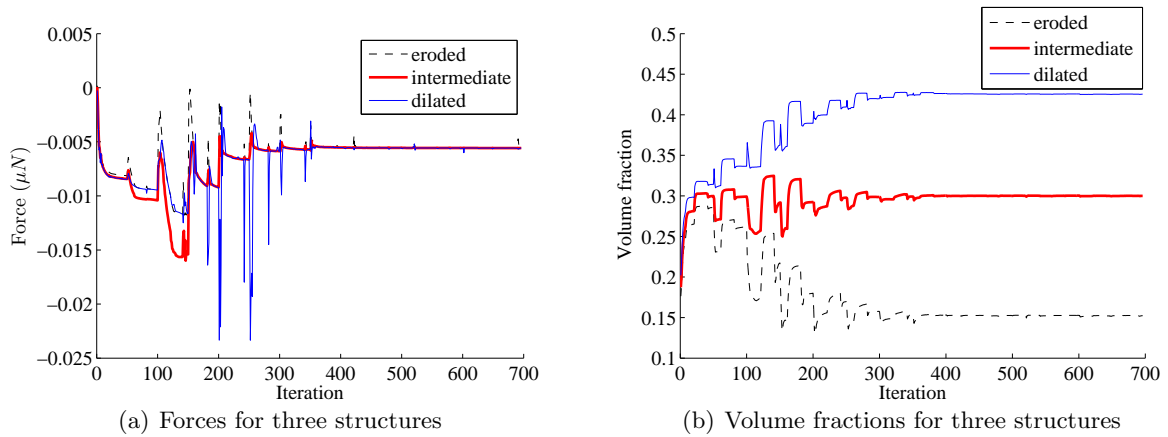


Figure 6: Forces and volume fractions of eroded, intermediate and dilated structures during iteration in optimizing the design with $R = 8.4h, \eta = 0.25$.

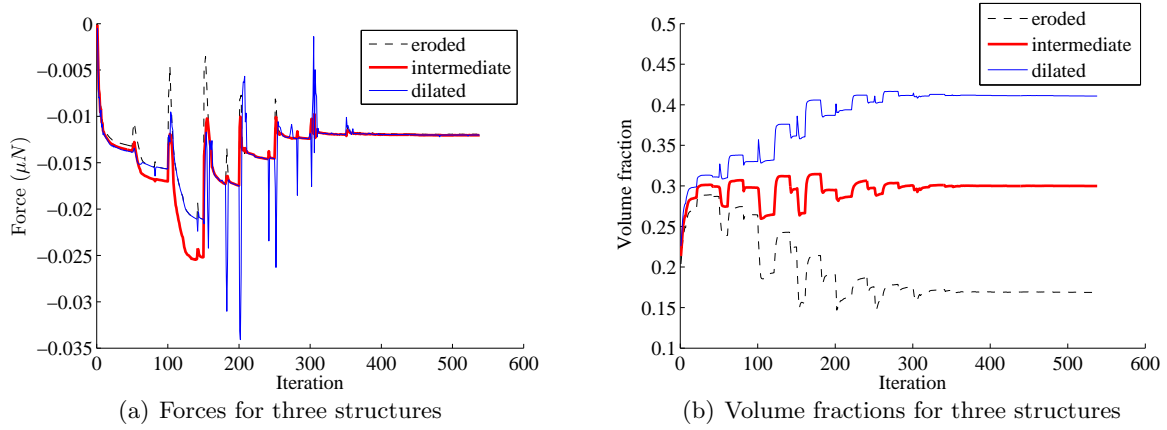


Figure 7: Forces and volume fractions of eroded, intermediate and dilated structures during iteration in optimizing the design with $R = 6.3h, \eta = 0.25$.

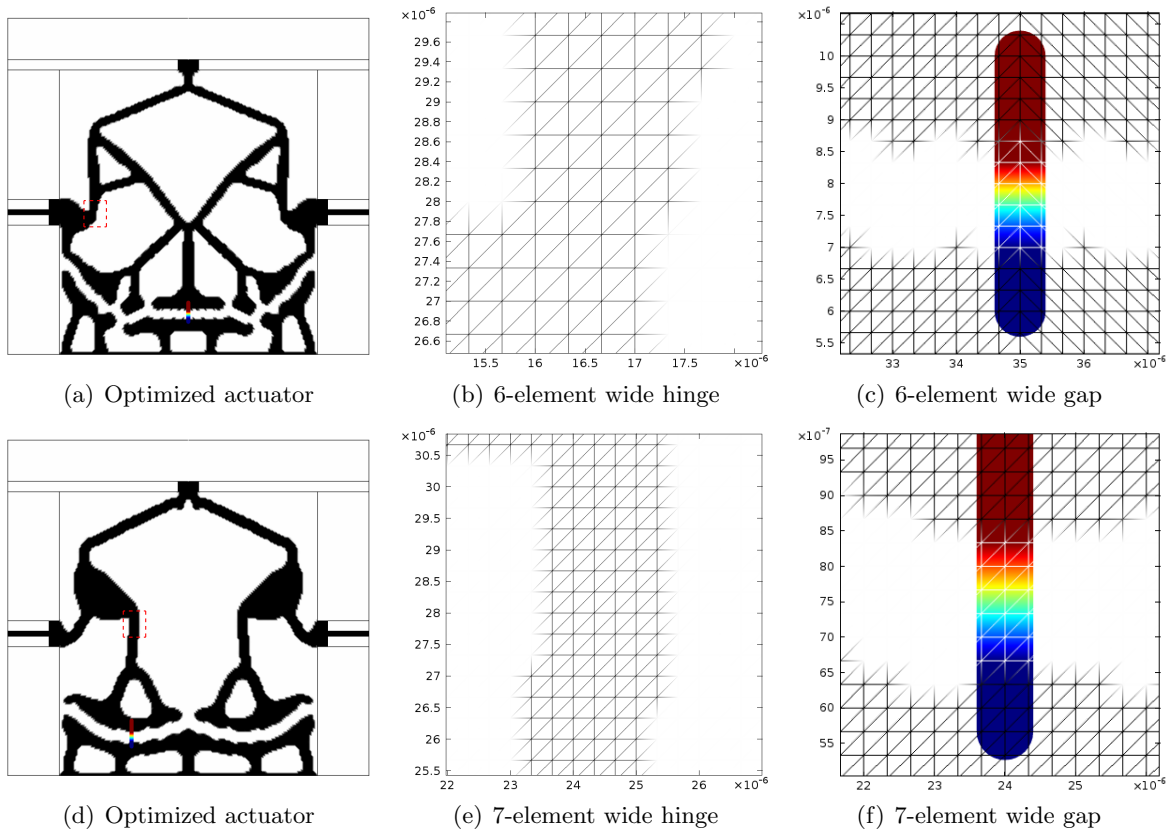


Figure 8: Robust formulation leads to minimal length control for both hinges and gaps for the designs shown in Fig. 4 and Fig. 5. Top row for design with $R = 6.3h$ and bottom row with $R = 8.4h$. The area around the dashed boxes in subfigures a) and d) are magnified in sub-figures b and e. The thin tubes in a) and d) are magnified in c and f.

Table 1 gives a quantitative comparison of predicted length ratio [14] and actual computed length scale, b/R , with respect to the threshold η for the inverter design, where b is the minimum feature length. An analytical formula (29) for predicting the minimal length scale b/R is given in the appendix, which is based on the assumption that the three structures controlled by the projection threshold $1 - \eta, 0.5, \eta$ are of the same topology and the underlying density filter is a simple hat function. The minimum feature length for the gap (the first number in the entries of Table 1) and for the hinge (the second number) are nearly identical and follow the predicted value reasonably well, even though our density filter is the Helmholtz PDE based filter. Note that, since the hinge and gap widths are measured in integers and counted by the element numbers, the maximum round-off error for $R_1 = 6.3h$ and $R_2 = 8.4h$ is respectively 16% and 12%. Figure 11 overlays the computed b/R values shown in Table 1 with the predicted b/R curve [14]. Accounting for the round-off error (shown as dashed curves in Fig. 11), the deviation between the predicted and computed length ratio is smaller than 1%. Note that the dashed lines are the offsets of one element above or below the predicted b/R curve, representing the computed minimal feature length's integer round-off error in b/R .

Table 1: Predicted and actual minimum length for the gap and hinge in the inverter designs

b/R	$\eta = 0.35$	$\eta = 0.25$	$\eta = 0.2$
Predicted [14]	0.77, 0.77	1.0, 1.0	1.11, 1.11
$R = 6.3h$	0.79, 0.63	0.95, 0.95	1.11, 0.95
$R = 8.4h$	0.60, 0.60	0.83, 0.83	1.07, 0.95

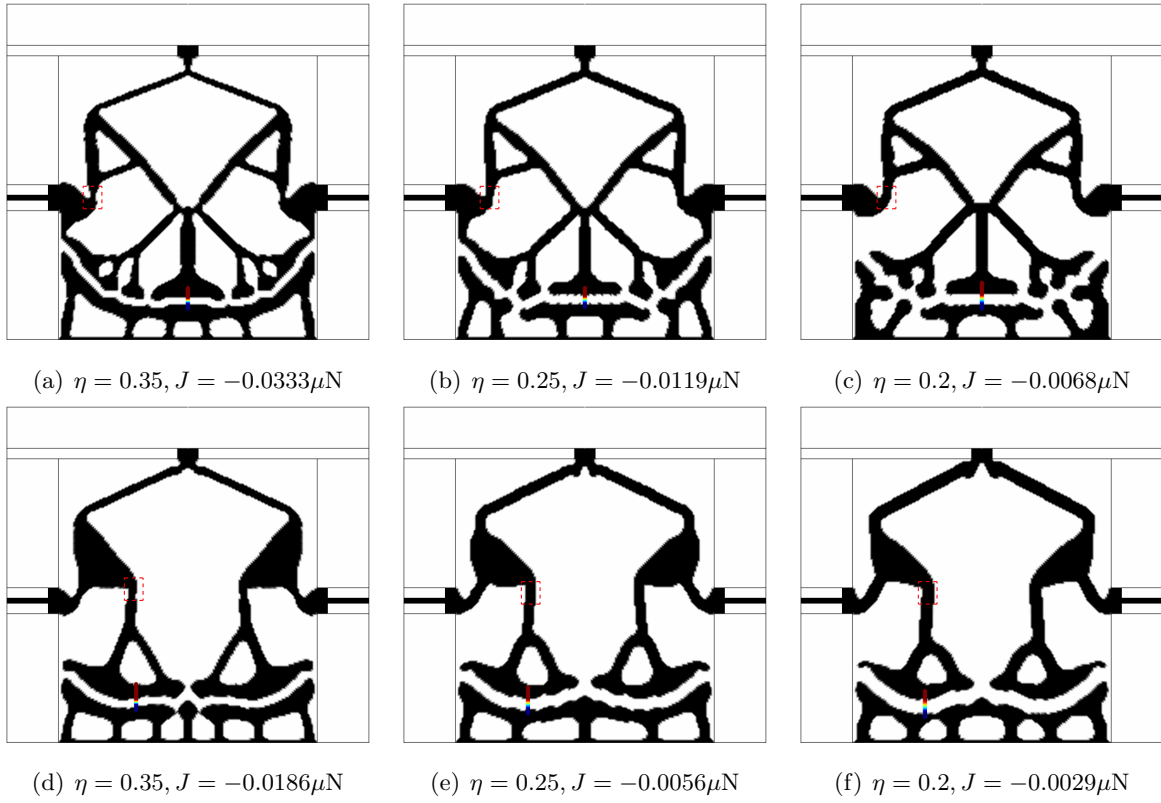


Figure 9: Optimized inverter designs for filter size $R = 6.3h$ (top row) and $R = 8.4h$ (bottom row). The dashed boxes indicate where the minimal hinge length is measured and the coloured thin tubes indicate where the gaps between electrodes are measured.

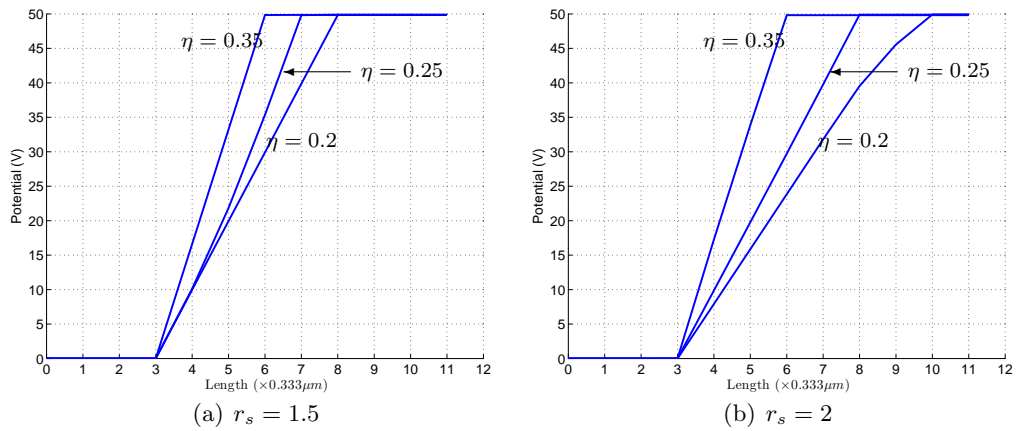


Figure 10: Electric potential across gaps for the $R = 6.3h$ and $R = 8.4h$ structures from Fig. 9.

material constants are the same as those for the inverter design.

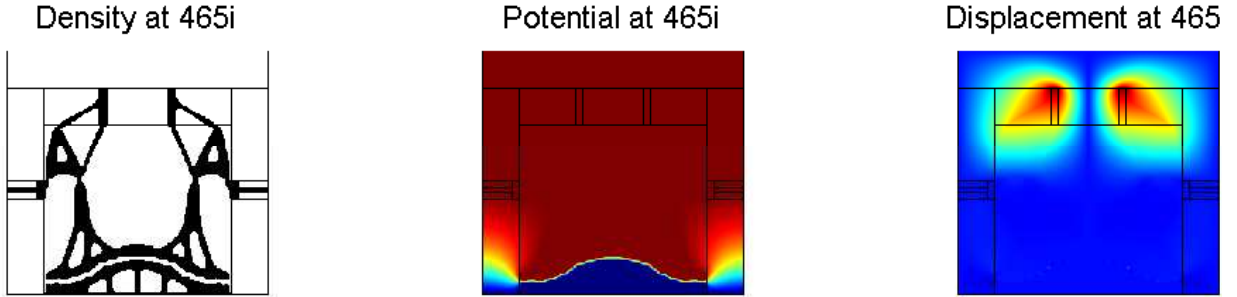


Figure 13: Optimized gripper design with $R = 5.6h, \eta = 0.25$.

An optimized design with the filter size $R = 5.6h$ and $\eta = 0.25$ and the corresponding electric potential and vertical displacement are shown in Fig. 13. This design took 465 iterations to converge. Figure 14 shows the obtained designs under different filter sizes R and Heaviside thresholds η . From this figure, we observe that with the increase of filter size and decrease of η , both minimal structural hinge sizes (as shown in the dashed boxes) and electrode gaps (as shown in the thin tube representing electric potential in the figure) are increasing. Figure 15 plots the electric potential transitions in the gaps. It further illustrates the length control via the filter radius R and projection threshold η . Table 2 quantitatively compares the predicted and actual computed ratio of the minimum feature length b with respect to the effective filter size R for a set of η values. The two rows are relative number b/R for the gap and the hinge. Figure 16 overlays the predicted length ratio b/R curve [14] and the computed minimal gap and hinge for various η and R combinations. It shows that the experimental results for the coupled problem match well with the prediction. Note that, for filter size of $R = 5.6h$ and $R = 7h$, the round-off errors for the hinge and gap measured in terms of element number are 18% and 14%. Excluding the round-off errors (shown as dashed lines in Figure 16), the deviation between the predicted length ratio b/R and the computed length ratio is within 1.6%. Note that the dashed lines are the offsets of one element above or below the predicted b/R curve, representing the computed minimal feature length's integer round-off error in b/R .

Table 2: Predicted and actual minimum length ratios (b/R) for the gap and hinge in the gripper designs

	$\eta = 0.35$	$\eta = 0.25$	$\eta = 0.15$
Predicted [14]	0.77, 0.77	1.0, 1.0	1.23, 1.23
$R = 5.6h$	0.89, 0.71	0.89, 1.07	1.43, 1.07
$R = 7h$	0.86, 0.71	1.00, 1.00	1.29, 1.29

It is clear that the gripper designs resulting from the robust topological filtering approach have controlled minimal length scales in both solids and voids and possess crisp boundary between solids

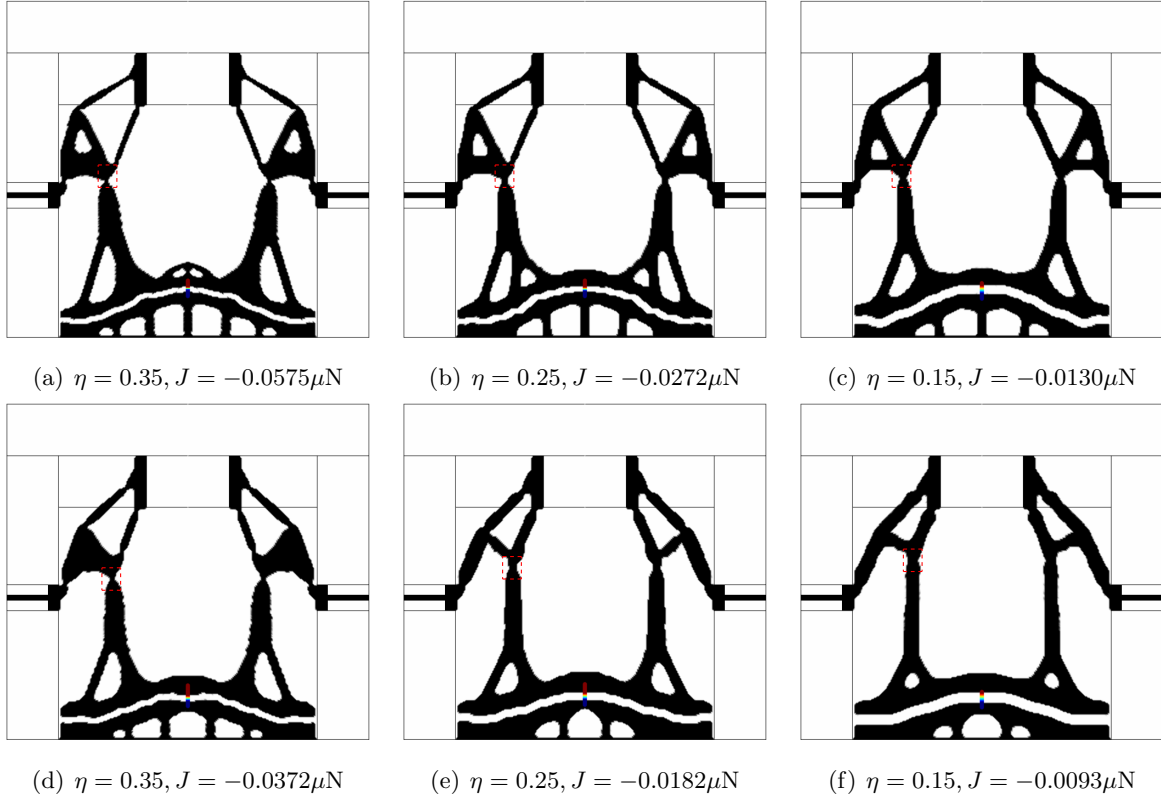


Figure 14: Optimized gripper designs under various parameters . Top row $R = 5.6h$ and bottom row $R = 7h$. The dashed boxes indicate where the minimal hinge length is measured and the coloured thin tubes indicate where the gaps between electrodes are measured.

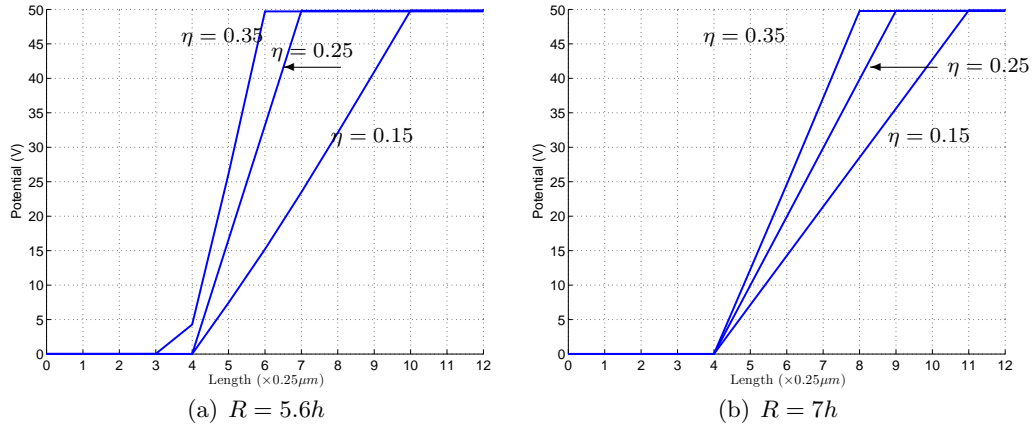


Figure 15: Electric potential across gaps for the structures optimized for $R = 5.6h$ and $R = 7h$ in Fig. 14.

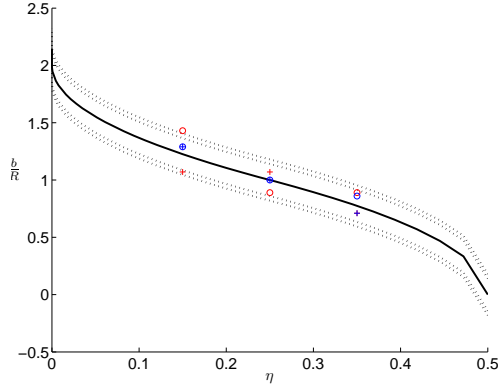


Figure 16: Comparison of predicted (solid line) and computed minimal gap (circles) and minimal hinge length (cross) under various η and R combinations for the gripper design. The dashed lines are the offsets of one element above or below the predicted b/R curve, representing the b 's integer round-off error in b/R .

and voids. The Helmholtz PDE based density filter coupled with the Heaviside filter in the robust three-structure formulation is effective in controlling the feature length. It thus effectively avoids the one-element hinge or gap issue that commonly exists in topological designs when the robust filter is not used.

5.3 Separate control for under- and over-etching

In the previous sections, we have demonstrated the robust control of minimal length in both solid structures and gaps by optimizing three structures. These three structures are obtained with three projection thresholds $\eta_e = 1 - \eta$, $\eta_i = 0.5$, $\eta_d = \eta$ respectively for eroded, intermediate and dilated structures, but they are controlled by one independent parameter η . As a result, the optimized structures exhibit the same minimal length scales in both solid structures and gaps. However, when the three structures are controlled by independent thresholds, η_e, η_i, η_d , one may control length scales of minimal structural and void details individually, thus leading to separate control for overcoming the manufacturing tolerance in under- and over-etching.

Figure 17 shows separate length control for guarding against different amount of under- and over-etching by independently controlling η_i and η_d . In the top row for the inverter design, where η_e is kept at 0.75 and η_d becomes larger and larger in these subfigures, ranging from 0.15 to 0.25 to 0.35, the minimal lengths of solids as shown in the dashed rectangles remain the same while the minimal lengths in electrode gaps become smaller. On the other hand, in the second row where η_e changes from 0.70 to 0.75 and 0.85 and η_d is kept at 0.25 for the gripper design, the minimal lengths in structures become larger and the minimal lengths in gaps remain the same. That is, independent control of η_e and η_d leads to separate length control for minimal lengths in solid structures and in gaps.

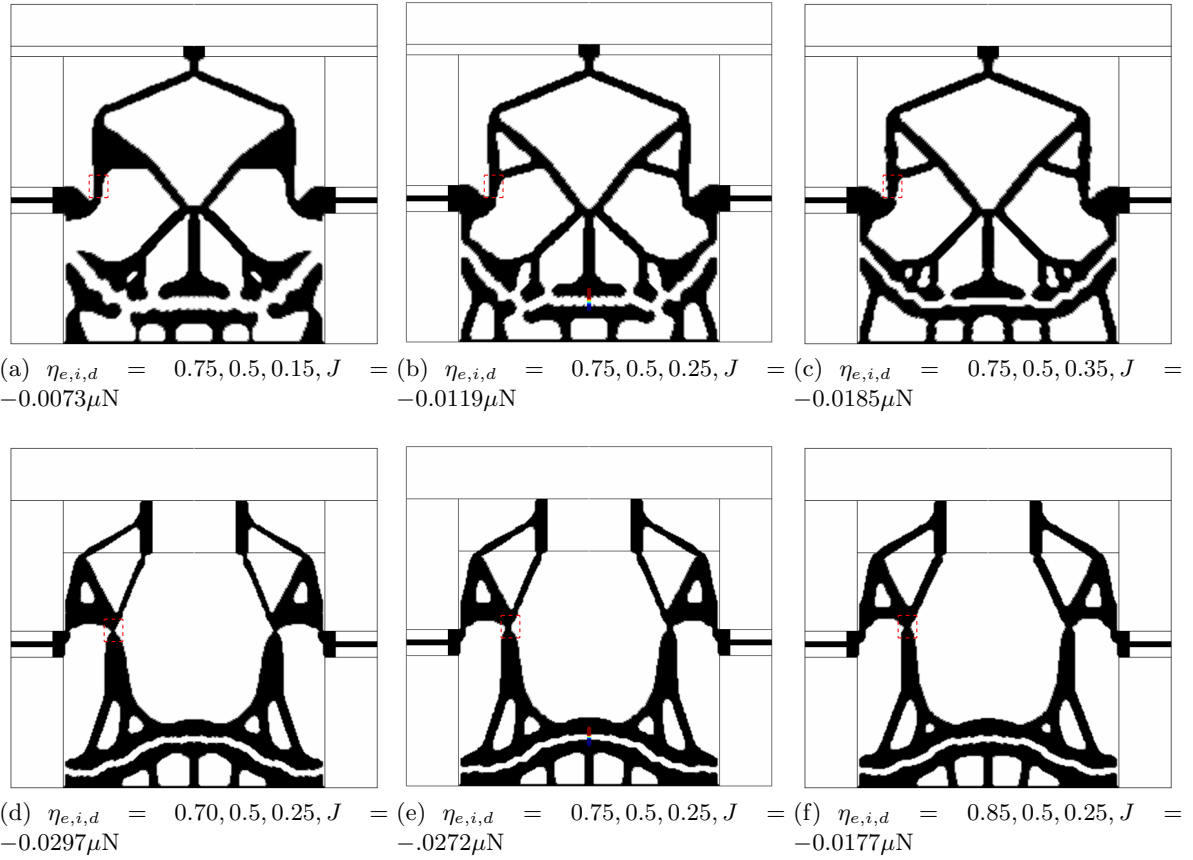


Figure 17: Separate length control for guarding against different amount of under-etching and over-etching by independently controlling η_i and η_d . From the left to the right, larger η_e leads to smaller minimal gaps and larger η_d leads to smaller minimal structures. Top row: inverter design. Bottom row: gripper design.

6 Conclusions

The paper presents a robust formulation for topology optimization of electromechanical actuators. Both inverters and grippers have been successfully optimized by this formulation. The optimized designs exhibit crisp structural boundaries and strict minimal length scale control. In particular, such minimal length control of both structural width and gap width avoids common modeling artifacts in topology optimization, i.e. one-element wide structure or gap, and thus leads to structures that are physically realizable and robust against manufacturing tolerances such as under-etching and over-etching. Further, our study finds that practically obtained minimum feature sizes agree remarkably well with the minimal length scales predicted through the numerical approach [14] or the analytical formula derived in the Appendix of this paper.

All the examples shown in the paper were run with the same parameters in a batch process. This means that for the used parameter settings the robust topology optimization approach provides very stable convergence and requires little parameter tuning. However, the tuning of the physical parameters for the electromechanic design problem has been more challenging. We find that the ratio between air and solid region Young’s modulus is rather critical for obtaining stable convergence. This, we attribute to our rather simplistic physical model and formulation of the optimization problem. With the wrong choice of physical parameters we encounter pull-in effects that destroy convergence. In order to circumvent such problems, one should use more sophisticated non-linear modeling schemes as e.g. suggested in [6, 8, 5]. However, since our main aim here is to show the potential advantages of the robust topology optimization strategy for use in advanced multiphysics applications, we have chosen not to consider these more advanced modeling issues here.

The robust formulation used here only considered manufacturing errors corresponding to over and under etching. Recent work for conventional compliant mechanism design has extended the robust formulation to spatially varying manufacturing errors [29] and it should be interesting to apply these ideas to the electromechanical actuators in the future.

Acknowledgements

The first author appreciates the support from the US National Science Foundation (grant 1200800). The second author appreciates the support from the Villum Foundation through the grant: “Next-Top.” We also thank Casper S Andreassen for his help in the initial stage of the Comsol implementation.

Appendix: Analytical formulas for predicting minimal length in robust formulation

This section derives analytical formulas for predicting the minimal length scale b as a function of the projection threshold η and the filter radius R for the three-structure robust formulation introduced in the papers by Sigmund’s [17] and Wang et al [14]. The assumption is that three structures controlled by the projection threshold $1 - \eta, 0.5, \eta$ are of the same topology and the underlying density filter is a simple hat function. Note that the analytical formulas is only possible due to the fact that the density is filtered via the normalized hat function, which can be described by a simple

convolution function $w_h = \frac{1}{R} \left(1 - \frac{|x|}{R}\right)$ over the domain $[-R, R]$ where R is the filter radius.

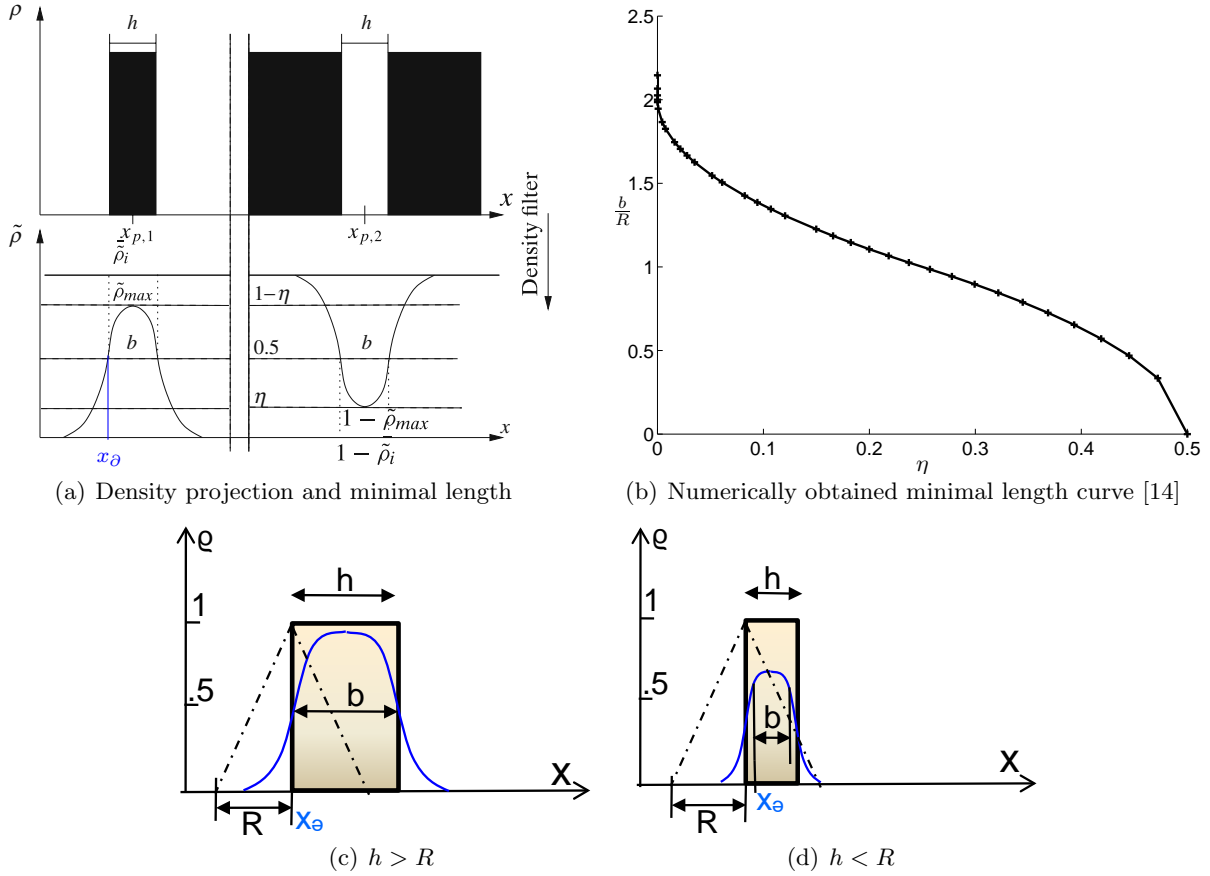


Figure 18: Minimal length prediction.

The way the minimal length is defined is shown in Fig. 18. For a given feature width h , when the maximum of the projected density $\tilde{\rho}_{\max}$ reaches η_e , the point with $\tilde{\rho} = \eta_i$ ($\eta_i = 0.5$) defines the boundary of the minimal width feature [14]. Corresponding to Fig. 18, we thus have the following expression for the filtered density $\tilde{\rho}(x)$ at the center $x_{p,1}$

$$\tilde{\rho}(x_{p,1}) = \int_{-h/2}^{h/2} \frac{1}{R} \left(1 - \frac{|x|}{R}\right) dx = \eta_e. \quad (27)$$

We note the point that defines the boundary of the intermediate structure as x_{∂} , i.e. the point with filtered density $\tilde{\rho}(x_{\partial}) \equiv \eta_i \equiv 0.5$. When the given feature size h is larger than the filter size R , as shown in Fig. 18c, the width b of the filtered feature with boundary density 0.5 equals to the given feature size h . When $h < R$, as shown in Fig. 18d, the filtered width is smaller than h .

Accordingly, we thus have the following expressions for the density at the boundary x_∂

$$\tilde{\rho}(x_\partial) = \int_0^R \frac{1}{R} \left(1 - \frac{|x|}{R}\right) dx = 0.5, \quad h \in [R, +\infty) \quad (28a)$$

$$\tilde{\rho}(x_\partial) = \int_0^{h-\frac{h-b}{2}} \frac{1}{R} \left(1 - \frac{|x|}{R}\right) dx + \int_{-\frac{h-b}{2}}^0 \frac{1}{R} \left(1 - \frac{|x|}{R}\right) dx = 0.5, \quad h \in [0, R] \quad (28b)$$

Equation (28a) describes the filtered density at the boundary of the intermediate structure where the structure width $h \geq R$ and equation (28b) describes the filtered density at the boundary of the intermediate structure where the structure width $h \leq R$. Solving (27) would lead to an expression of h in terms of η_e and plugging it into (28), we can then obtain the expression for minimal width ratio b/R as follows

$$\frac{b}{R} = \begin{cases} 2 - 2\sqrt{1 - \eta_e}, & \eta_e \in [0.75, 1] \\ 2\sqrt{\eta_e - 1/2}, & \eta_e \in [0.5, 0.75] \end{cases} \quad (29)$$

Equation (29) gives the length expression for an input η_e . Figure 19 overlaps the length curve b/R versus $(1 - \eta_e)$ from (29) with the curve obtained numerically in [14]. It shows agreement.

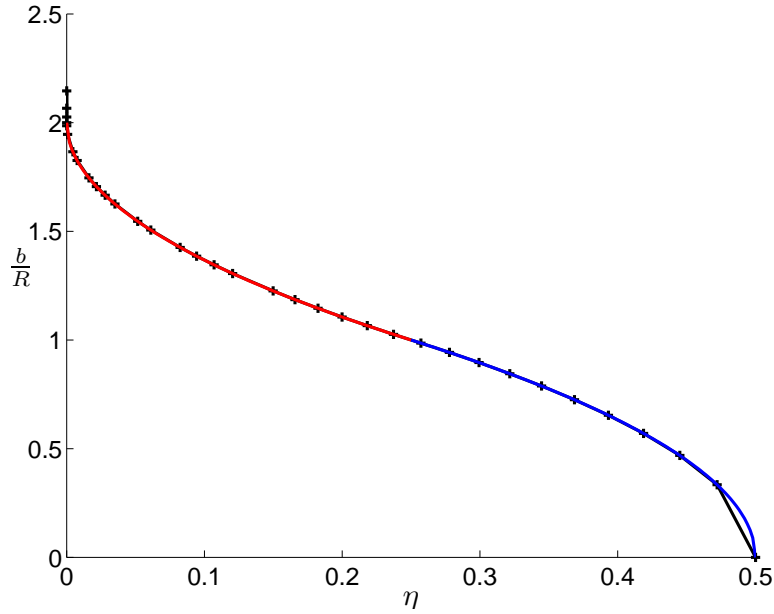


Figure 19: Overlay of analytical length curve with numerically obtained curve in [14].

We can also rewrite (29) into the following form

$$\eta_e = \begin{cases} \frac{1}{4} \left(\frac{b}{R}\right)^2 + \frac{1}{2}, & \frac{b}{R} \in [0, 1] \\ -\frac{1}{4} \left(\frac{b}{R}\right)^2 + \frac{b}{R}, & \frac{b}{R} \in [1, 2] \\ 1, & \frac{b}{R} \in [2, +\infty) \end{cases} \quad (30)$$

Equation (30) is useful for design where, for a desired minimal width b and a given filter radius R , one wants to find the corresponding η_e . Figure 20 plots the η_e and b/R curve.

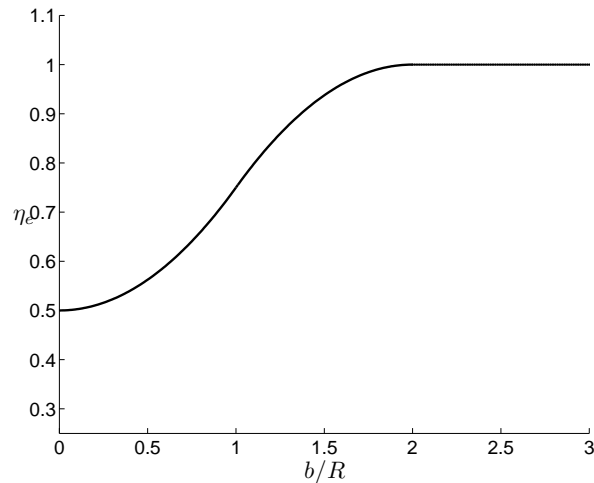


Figure 20: The η versus b/R curve useful for design.

References

- [1] M.P. Bendsøe and N. Kikuchi. Generating optimal topologies in structural design using a homogenization method. *Computer methods in applied mechanics and engineering*, 71(2):197–224, 1988.
- [2] M.P. Bendsøe and O. Sigmund. *Topology optimization: theory, methods, and applications*. Springer Verlag, 2003.
- [3] O. Sigmund. Design of multiphysics actuators using topology optimization-part i: One-material structures. *Computer methods in applied mechanics and engineering*, 190(49-50):6577–6604, 2001.
- [4] G.H. Yoon, J.S. Jensen, and O. Sigmund. Topology optimization of acoustic–structure interaction problems using a mixed finite element formulation. *International journal for numerical methods in engineering*, 70(9):1049–1075, 2007.
- [5] E. Lemaire, P. Duysinx, V. Rochus, and J.C. Golinval. Improvement of pull-in voltage of electromechanical microbeams using topology optimization. In *III European Conference on Computational Mechanics*, pages 488–488. Springer, 2006.
- [6] V. Rochus, D.J. Rixen, and J.C. Golinval. Monolithic modelling of electro-mechanical coupling in micro-structures. *International journal for numerical methods in engineering*, 65(4):461–493, 2006.

- [7] Z. Liu, J.G. Korvink, and M.L. Reed. Multiphysics for structural topology optimization. *Sensor Letters*, 4(2):191–199, 2006.
- [8] M. Rauli and K. Maute. Topology optimization of electrostatically actuated microsystems. *Structural and Multidisciplinary Optimization*, 30(5):342–359, 2005.
- [9] L. Yin and GK Ananthasuresh. A novel topology design scheme for the multi-physics problems of electro-thermally actuated compliant micromechanisms. *Sensors and Actuators A: Physical*, 97:599–609, 2002.
- [10] G.H. Yoon and O. Sigmund. A monolithic approach for topology optimization of electrostatically actuated devices. *Computer Methods in Applied Mechanics and Engineering*, 197(45-48):4062–4075, 2008.
- [11] K.C. David. *Field and Wave Electromagnetics*. Addison-Wesley Publishing Company, Inc., Massachusetts, USA, 1990.
- [12] J. Byun, I. Park, and S. Hahn. Topology optimization of electrostatic actuator using design sensitivity. *Magnetics, IEEE Transactions on*, 38(2):1053–1056, 2002.
- [13] J.H. Kuang and C.J. Chen. The nonlinear electrostatic behavior for shaped electrode actuators. *International journal of mechanical sciences*, 47(8):1172–1190, 2005.
- [14] F. Wang, B.S. Lazarov, and O. Sigmund. On projection methods, convergence and robust formulations in topology optimization. *Structural and Multidisciplinary Optimization*, 43:767–784, 2011.
- [15] K.J. Bathe. *Finite element procedures*. Englewood Cliffs, New Jersey, 1996.
- [16] Ole Sigmund. Morphology-based black and white filters for topology optimization. *Structural and Multidisciplinary Optimization*, 33:401–424, 2007. 10.1007/s00158-006-0087-x.
- [17] O. Sigmund. Manufacturing tolerant topology optimization. *Acta Mechanica Sinica*, 25(2):227–239, 2009.
- [18] JK Guest, JH Prévost, and T. Belytschko. Achieving minimum length scale in topology optimization using nodal design variables and projection functions. *International Journal for Numerical Methods in Engineering*, 61(2):238–254, 2004.
- [19] Shengli Xu, Yuanwu Cai, and Gengdong Cheng. Volume preserving nonlinear density filter based on heaviside functions. *Structural and Multidisciplinary Optimization*, 41:495–505, 2010. 10.1007/s00158-009-0452-7.
- [20] N. Olhoff. Multicriterion structural optimization via bound formulation and mathematical programming. *Structural and Multidisciplinary Optimization*, 1(1):11–17, 1989.
- [21] K. Svanberg. The method of moving asymptotes: A new method for structural optimization. *International Journal of Numerical Methods in Engineering*, 24:359 – 373, 1987.
- [22] Laurits H. Olesen, Fridolin Okkels, and Henrik Bruus. A high-level programming-language implementation of topology optimization applied to steady-state navier-stokes flow. *International Journal of Numerical Methods in Engineering*, 65:9751001, 2006.

- [23] K. Matsui and K. Terada. Continuous approximation of material distribution for topology optimization. *International Journal for Numerical Methods in Engineering*, 59(14):1925–1944, 2004.
- [24] S. F. Rahmatalla and C. C. Swan. A Q4/Q4 continuum structural topology optimization implementation. *Structural and Multidisciplinary Optimization*, 27:130–135, 2004.
- [25] Atsushi Kawamoto, Tadayoshi Matsumori, Shintaro Yamasaki, Tsuyoshi Nomura, Tsuguo Kondoh, and Shinji Nishiwaki. Heaviside projection based topology optimization by a PDE-filtered scalar function. *Structural and Multidisciplinary Optimization*, pages 1–6, 2010. 10.1007/s00158-010-0562-2.
- [26] BS Lazarov and O. Sigmund. Filters in topology optimization based on Helmholtz-type differential equations. *International Journal for Numerical Methods in Engineering*, 86(6):765–781, 2011.
- [27] E. Andreassen, A. Clausen, M. Schevenels, B. Lazarov, and O. Sigmund. Efficient topology optimization in matlab using 88 lines of code. *Structural and Multidisciplinary Optimization*, 43:1–16, 2011. MATLAB code available online at: www.topopt.dtu.dk.
- [28] J. Fish and T. Belytschko. *A First Course in Finite Elements*. John Wiley and Sons, Ltd, 2007.
- [29] M. Schevenels, B.S Lazarov, and O. Sigmund. Robust topology optimization accounting for spatially varying manufacturing errors. *Computer Methods in Applied Mechanics and Engineering*, 200(49-52):3613–3627, 2011.